

Recent results from Super-Kamiokande

Yusuke Koshio
for Super-Kamiokande collaboration

Kamioka Observatory, Institute for Cosmic Ray Research
Higashi-Mozumi Kamioka-cho, Yoshiki-gun, Gifu 506-1205, Japan

March 5th , 1998

Abstract

Preliminary results on atmospheric neutrinos and solar neutrinos in Super-Kamiokande are presented. The results re-confirmed the atmospheric neutrino anomaly and the solar neutrino problem. The neutrino oscillations, which is a possible solution of these problems, are also studied.

1 Super-Kamiokande detector

Super-Kamiokande is a ring imaging water Cherenkov detector. Cherenkov lights generated by charged particles scattered by neutrinos in water are detected by 20-inch photomultiplier tubes (PMT).

In a medium with an index of refraction of n , the light velocity is c/n . When a charged particle traverses the medium with velocity larger than the light velocity, so called Cherenkov light is emitted. Cherenkov light is emitted in a cone of half angle θ from the direction of the particle track:

$$\cos \theta = \frac{1}{n\beta}, \quad (1)$$

where $\beta = v/c$, and θ is 42° for $\beta = 1.0$ in water. Therefore, the pattern detected by PMTs becomes ring image.

The detector consists of about 50000 tons of pure water filled in a cylindrical water tank (diameter 39.3m and height 41.4m), a water and air purification system, PMTs, electronics and online data acquisition system, and offline computer facilities. Fig 1 shows a schematic view of the detector. It is located 1000m underground (2700m of water equivalent) in the Kamioka mine in Gifu Prefecture, Japan.

The reason that the detector is underground is to shield against cosmic ray muons. Compared to ground level, the intensity of muons is reduced by about 10^{-5} at the depth of the Super-Kamiokande detector. The muon rate in Super-Kamiokande is about 2Hz.

The water tank is made of stainless steel, and it is divided into an inner part and an outer part. These are summarized in Table 1. The reason for the division is mainly to identify remaining muon events from outside the tank and to reject gamma rays and neutrons from the rock.

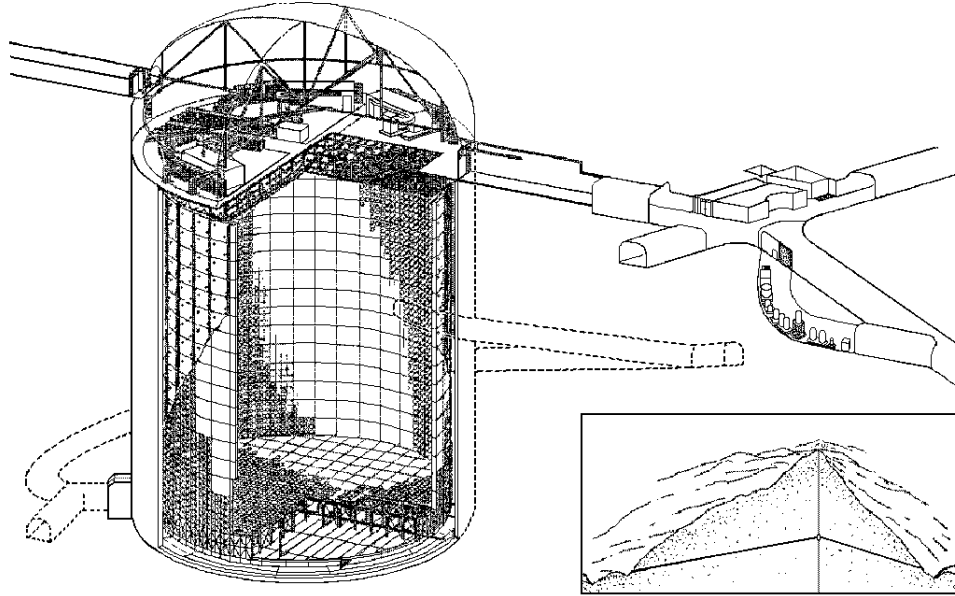


Figure 1: The detector appearance. Inset at bottom right shows the location within the mountain. (cutaway view)

Tank	Dimensions Volume	39.3m in diameter \times 41.4m in height 50 kton
Outer part	Thickness Volume Num. of PMT	2.6m on top and bottom 2.75m on barrel 32 kton 302 (top), 308 (bottom) and 1275 (barrel)
Inner part	Dimensions Volume Num. of PMT	33.8m in diameter \times 36.2m in height 18 kton 1748 (top and bottom) and 7650 (barrel)
Fiducial area	Thickness Volume	2m from the inner wall 22kton

Table 1: Several parameters of Super-Kamiokande detector.

The tank is sealed tightly to keep the mine's radon rich air from entering. Radon gas is the most serious background for the solar neutrino analysis. The concentration of radon gas in the dome air is about 1500 Bq/m³ in summer time and 30 Bq/m³ in winter time. This large difference is caused by the flow of air in the mine. Air blows into the mine in the winter and out of the mine in the summer. After the effort to remove radon gas from the water, the radon concentration in the water decreases to the level of 5~10mBq/m³.

We use 11146 20-inch PMTs in the inner detector and 1885 8-inch PMTs in the outer detector. This is summarized in Table 1. In the inner detector, PMTs are placed at intervals of 70 cm, and the ratio of PMT area to all area (photo coverage) is 40.41%. The wall of the tank is covered with black polyethylene terephthalate sheets (called "black sheet") behind the inner PMTs. In the outer detector, there are 2 outer PMTs in the region behind each 12 inner PMTs, and they face outward from the support structure. Around each outer PMT, there is wave length shifter to increase photo coverage. In order to increase the light detection efficiency, all surfaces of the outer detector are covered with white tyvek sheets with a reflectivity of above 80%. The inner part and outer part are optically isolated using black sheets and tyvek sheets. There are complicated stainless steel frames for supporting the PMTs and so on in this optically insensitive region.

Construction started in 1991. First, the cavity was excavated until the middle of 1994. After that, water tank construction started, and it finished in the middle of 1995. From June of 1995, we installed PMTs and set the electronics system simultaneously. This continued until the end of 1995. Water filling was from January to March in 1996. After a 1 month test run, we started normal data taking from April 1st in 1996. In this paper, the results of about 400days of data, which is from May in 1996 to October in 1997, are reported.

2 Preliminary results of atmospheric neutrinos

2.1 Atmospheric neutrino anomaly

Atmospheric neutrinos are the decay products of mesons created by interactions of primary cosmic rays in the atmosphere. The following decay chain is dominant.

$$\begin{aligned} \pi^\pm &\rightarrow \mu^\pm + \nu_\mu(\bar{\nu}_\mu) \\ &\downarrow \\ \mu^\pm &\rightarrow e^\pm + \nu_e(\bar{\nu}_e) + \nu_\mu(\bar{\nu}_\mu). \end{aligned}$$

The uncertainty in the calculation of atmospheric neutrino flux is estimated to be ~30%, however, the ratio of the number of ν_μ and ν_e is calculated to be 2:1 with ~5% uncertainty. Super-Kamiokande observe electrons and muons produced by the reaction, for example, $\nu_l N \rightarrow l N'$, where l shows electron or muon. The double ratio, $R = (\mu/e)_{DATA}/(\mu/e)_{MC}$, is calculated, and it cancels many uncertainties. The results of the current experiments is shown in Table 2. The data is significantly smaller than Monte Carlo in several experiments[1].

In addition of that, the measurement of the particle direction is available in Kamiokande and Super-Kamiokande. There are large difference of the neutrino flight length between downward (10~30km) and upward (~13000km). The zenith angle dependence can check the effect of neutrino oscillation.

Experiment	exposure (kt·yr)	events	R
NUSEX	0.74	50	$0.96^{+0.32}_{-0.28}$
Frejus	2.0	200	$1.00 \pm 0.15 \pm 0.08$
Kamiokande sub-GeV	7.7	482	$0.60^{+0.06}_{-0.05} \pm 0.05$
Kamiokande multi-GeV	6/8.2	233	$0.57^{+0.08}_{-0.07} \pm 0.07$
IMB	7.7	610	$0.54 \pm 0.05 \pm 0.11$
Soudan-II	2.83	331	$0.61 \pm 0.14^{+0.05}_{-0.07}$
Super-K sub-GeV	25.5	2579	$0.610 \pm 0.03 \pm 0.05$
Super-K multi-GeV	25.5	792	$0.659 \pm 0.06 \pm 0.08$

Table 2: Measurements of the double ratio R in several atmospheric neutrino experiments.

2.2 Atmospheric neutrino analysis

2.2.1 Data reduction

The data used for the atmospheric neutrino analysis covers from May 1996 to October 1997. The total analysis live time is 414 days, which is equivalent to 25.5 kton·year. First, the atmospheric neutrino events are classified into fully contained (FC) events and partially contained (PC) events. The FC events are selected by requiring no hits in the outer detector. The PC events are selected by requiring hit cluster in the outer detector close to an exit point of the particles observed in the inner detector.

Fig 2 shows the analysis steps and the event rate at each step. The reduction and scan in the figure are to select the events with the energy for atmospheric neutrino analysis and to reject several noise events. The final sample is divided by the energy region. The events with less than 1.33GeV is called to sub-GeV events and with greater than 1.33GeV is multi-GeV events.

The event reconstruction shown in Fig 2 means counting the number of rings, particle identification, momentum reconstruction, and so on. The particle identification makes use of the pattern of the Cherenkov ring. Electrons produce electromagnetic showers and rather diffuse Cherenkov rings, while muons produce sharp Cherenkov edges. We identify these events using likelihood method and classify e-like and μ -like events. The probability of mis-identification is $\sim 1\%$ for sub-GeV events and $\sim 2\%$ for multi-GeV events.

2.2.2 Results

Table 3 shows the event summary of sub-GeV and multi-GeV atmospheric neutrino analysis. The double ratio in the sub-GeV events is

$$\frac{(\mu/e)_{DATA}}{(\mu/e)_{MC}} = 0.610 \pm 0.03 \pm 0.05 \quad (\text{sub-GeV}). \quad (2)$$

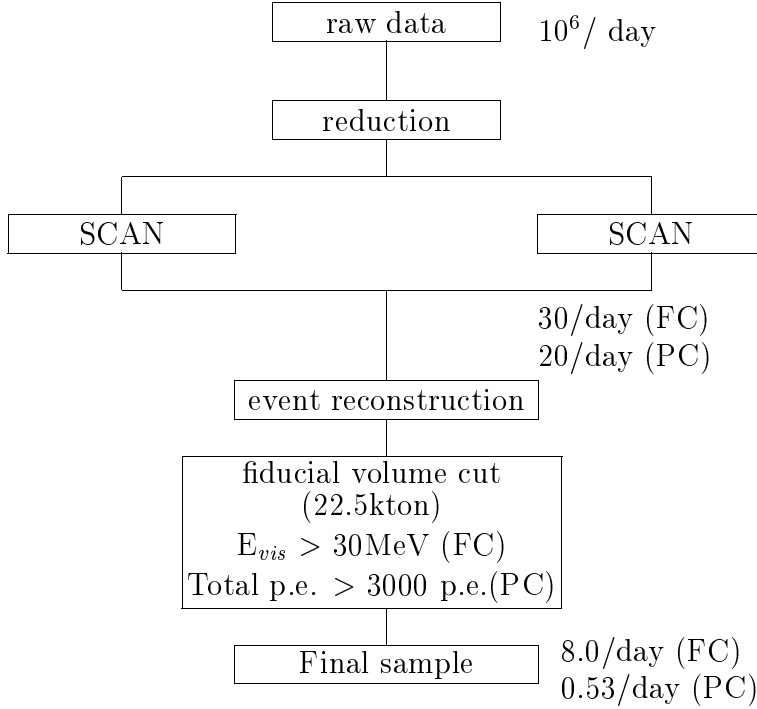


Figure 2: The analysis steps in atmospheric neutrino events.

The double ratio in the multi-GeV events is

$$\frac{(\mu/e)_{DATA}}{(\mu/e)_{MC}} = 0.659 \pm 0.06 \pm 0.08 \quad (\text{multi-GeV}). \quad (3)$$

Here, we use the flux calculation by Honda et al.[2] as the Monte Carlo simulation. The double ratios of the data are significantly smaller than Monte Carlo both in sub-GeV and multi-GeV events, and consistent with the results of Kamiokande.

Fig 3 shows the zenith angle distribution of the observed e-like and μ -like events. From the figure, we can see that the upward-going μ -like events are significantly smaller than the MC expectations. It is shown both in sub-GeV and multi-GeV events. Fig 4 shows the zenith angle dependence of the double ratio, R . The double ratio is depend on the zenith angle as shown in the figure. This distortion of the zenith angle distribution strongly indicates anomaly in the atmospheric neutrino, because the upward-downward asymmetry of the detector is negligibly small. Fig 5 shows the momentum distribution and no momentum dependence can be seen.

2.2.3 Implication of the atmospheric neutrino anomaly

As described above, the atmospheric neutrino anomaly was re-confirmed by Super-Kamiokande. It is that the double ratio, R , is significant smaller than unity, and the zenith angle distortion. Those results strongly indicates neutrino oscillation. Using the results, an allowed region of neutrino oscillation parameters assuming $\nu_\mu \leftrightarrow \nu_\tau$ oscillations is calculated. That is shown

sub-GeV

	DATA	Monte Carlo
1 ring	1883	2030.5
e-like	983	812.2
μ -like	900	1218.3
2 ring	562	604.3
≥ 3 ring	134	154.9
Total	2579	2789.7

multi-GeV

FC	DATA	Monte Carlo
1 ring	394	411.6
e-like	218	182.7
μ -like	176	229.0
2 ring	212	229.0
≥ 3 ring	186	204.6
Total	792	845.2
PC	230	287.7

Table 3: Summary of sub-GeV and multi-GeV events compared with the Monte Carlo simulation.

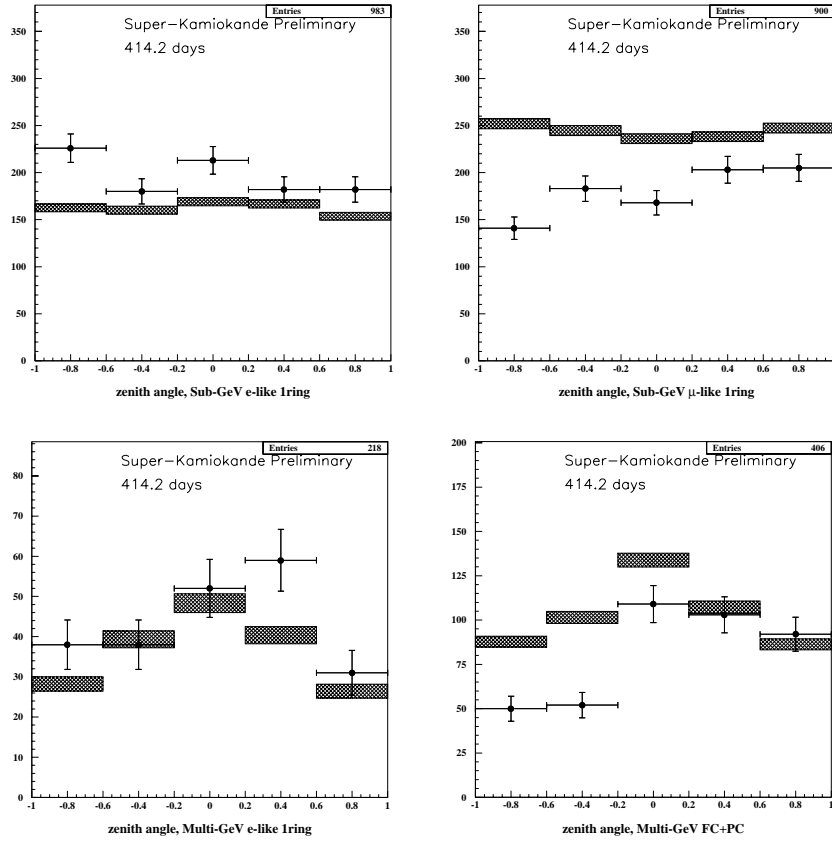


Figure 3: The zenith angle distribution of the observed e-like and μ -like events in Super-Kamiokande. Upper and lower figures are for sub-GeV and multi-GeV data, respectively. The horizontal axis shows the cosine of the zenith angle. 1 corresponds to downward and -1 corresponds to upward. The hatched bands shows the MC simulation.

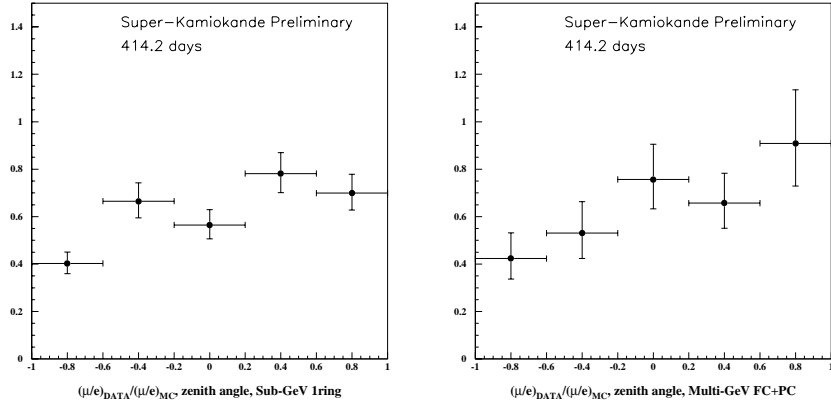


Figure 4: The zenith angle dependence of the double ratio. The left and right figures show the sub-GeV and multi-GeV data, respectively. The horizontal axis shows the cosine of the zenith angle, and the vertical axis shows the double ratio.

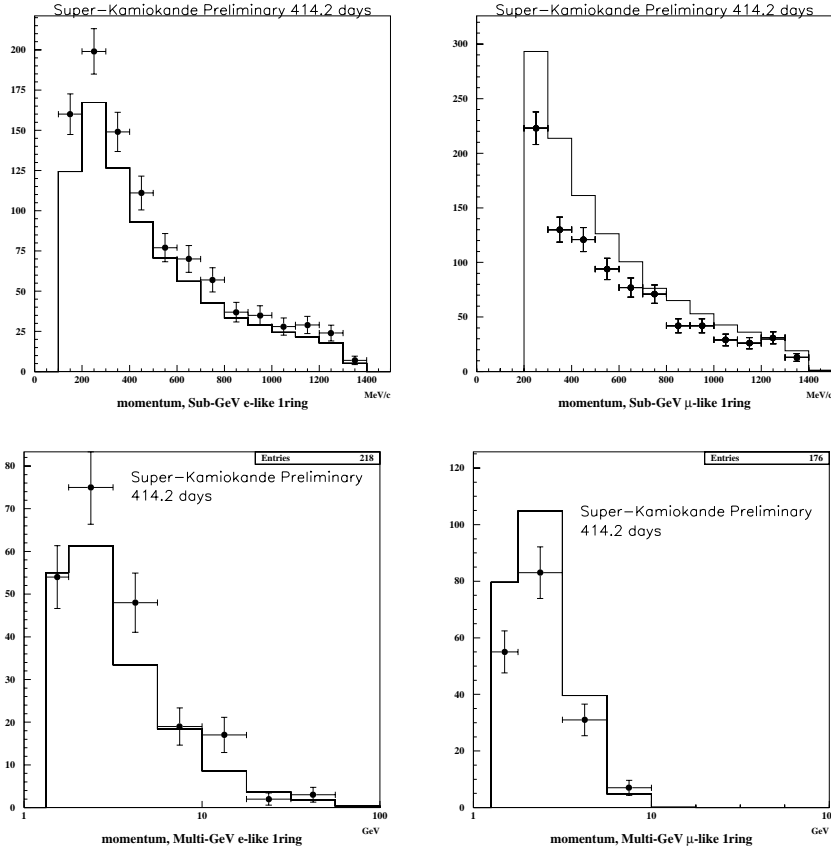


Figure 5: The momentum distribution of the observed e-like and μ -like events in Super-Kamiokande. Upper and lower figures are for sub-GeV and multi-GeV data, respectively.

in Fig 6. The overlapped allowed region of Super-Kamiokande and Kamiokande is around $\Delta m^2 = 10^{-3} \sim 10^{-2} \text{ eV}^2$ and $\sin^2 2\theta = 0.8 \sim 1.0$.

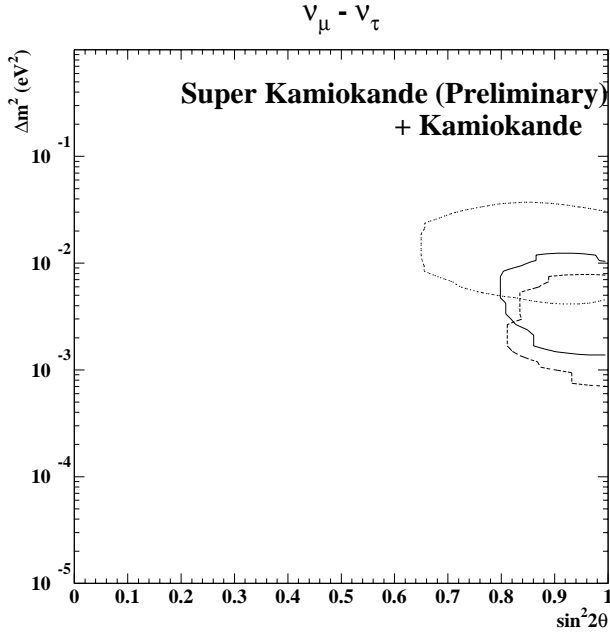
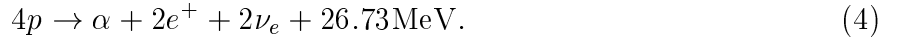


Figure 6: Allowed region of neutrino oscillation parameters with 90% C.L. obtained by atmospheric neutrino data in Super-Kamiokande (lower dashed line) and Kamiokande (upper dashed line). The solid line shows the combined results of Super-Kamiokande and Kamiokande.

3 Preliminary results of solar neutrinos

3.1 Solar neutrino problem

The origin of the energy in the sun is the following nuclear fusion reaction,



In the center of the sun, reaction(4) is realized through the reaction chains : pp-chains and CNO cycle. With the current knowledge of the temperature of the sun, the pp chain is believed to be dominant. The neutrinos from each reaction in the pp chain in Fig 7 are called: (1) pp neutrinos, (2) pep neutrinos, (3) ${}^7\text{Be}$ neutrinos, (4) ${}^8\text{B}$ neutrinos, and (5) hep neutrinos. Only ${}^8\text{B}$ neutrinos and hep neutrinos can be detected in Super-Kamiokande, but the expected rate from hep neutrinos is very small.

The neutrino fluxes and spectra in these reactions are predicted by so called Standard Solar Models (SSMs). We use “BP95”, which was published by Bahcall and Pinsonneault in 1995[3] among the several SSMs.

The results of the current solar neutrino flux is shown in Table 4. In all the solar neutrino experiments up to now, the observed flux is significantly smaller than expected flux[4]. This is called “the solar neutrino problem”.

Various explanations of the solar neutrino problem have been proposed. Those approaches are mainly classified (1) the modification of the SSM, and (2) the not-yet resolved properties

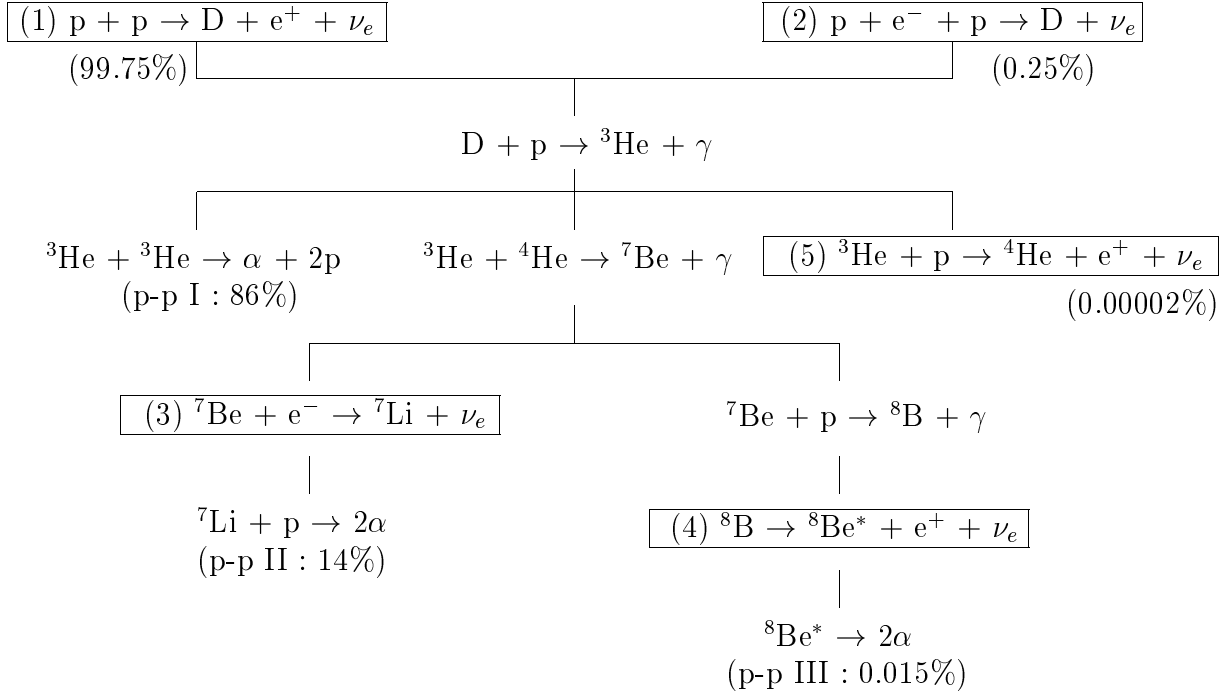


Figure 7: Proton-proton chain.

Experiment	Detection method	Energy threshold	DATA/SSM (BP95)
Homestake	$^{37}\text{Cl}(\nu_e, e^-)^{37}\text{Ar}$	0.814MeV	$0.273 \pm 0.015 \pm 0.015$
Kamiokande	$\nu_e + e^- \rightarrow \nu_e + e^-$	7.0MeV	$0.423 \pm 0.029 \pm 0.050$
GALLEX			$0.556 \pm 0.047 \pm 0.036$
SAGE	$^{71}\text{Ga}(\nu_e, e^-)^{71}\text{Ge}$	0.233MeV	$0.504 \pm 0.073^{+0.036}_{-0.051}$

Table 4: The summary of several solar neutrino experiments and the results.

of neutrinos, especially the MSW effect [5] in neutrino oscillations. The most effective method to solve the problem is an independent measurement on solar models, because SSMs have been improved but the flux calculation from SSMs has remained ambiguous. Super-Kamiokande can measure the energy spectrum and the time dependence of the solar neutrino flux, (day-night or seasonal flux differences). These are solar model independent measurements of solar neutrinos.

3.2 Solar neutrino analysis

3.2.1 Detector calibration

In the observation of solar neutrinos in Super-Kamiokande, recoil electrons through the following reaction are measured;

$$\nu + e^- \rightarrow \nu + e^- . \quad (5)$$

Therefore, we use mainly mono-chromatic electron sources from a linear accelerator (LINAC) as the detector calibration. For the solar neutrino analysis, the energy calibration at several energies (around 4MeV to 17MeV) and positions is most important. The incident electron energy from LINAC is determined by germanium detector with less than 20keV. The Monte Carlo is tuned by LINAC data and the energy is determined by this tuned Monte Carlo. The differences between the real data and the Monte Carlo is shown in Fig 8. The energy dependence of the difference is less than $\pm 0.3\%$ for energy region above the analysis threshold (6.5MeV). The position dependence leads $\pm 0.3\%$ systematic error in an extrapolation of the energy scale determined at six positions to the entire fiducial volume.

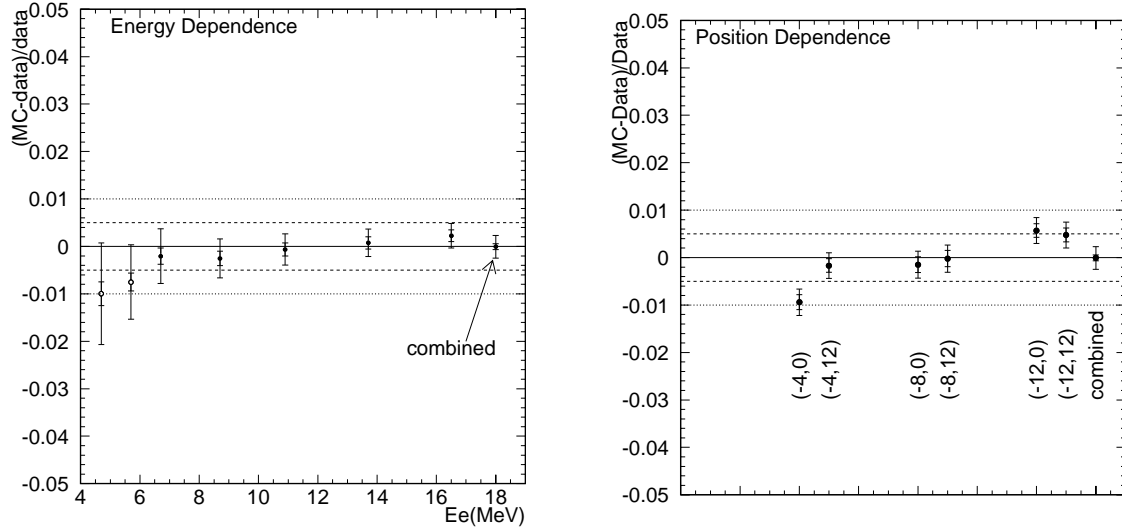


Figure 8: The difference of energy scale between data and Monte Carlo. The left figure shows the energy dependence and the right one shows the position dependence.

3.2.2 Data reduction

The data used for the solar neutrino analysis covers from May 1996 to October 1997. The total analysis live time is 374.2 days. Table 5 shows the number of events remaining at each step. The first and second reduction is to select the events with less than 20MeV (which is the solar neutrino energy region) and to reject several noise events. Next, we take spallation cut. When an energetic muon go through the tank, it breaks Oxygen in the water and produces several radioactive elements. The spallation products give β and/or gammas in the energy range between a few MeV and 20MeV. This energy region is near the energy of solar neutrino events, so spallation events are one of the major backgrounds for solar neutrino analysis. These events have time and spatial correlations with muon track, and they are correlated with total charge of muon event. Using the above information, we eliminate spallation events. Finally, we take gamma cut. The gamma rays from the surrounding rocks become serious backgrounds for solar neutrino analysis. Using the information of the position and direction, we reduce this background events.

LOW-ENERGY DATA REDUCTION
MAY 31, 1996 ~ OCT. 20, 1997
Live time 374.2 days

reduction step	number of events	
	Data	Monte Carlo
RAW DATA	$\sim 4 \times 10^8$	6.2×10^6
First reduction		
Total charge ≤ 1000 p.e.	2.98×10^8	(797028)
Time to previous event $> 20\mu\text{sec}$.	2.56×10^8	
Event status flag	2.52×10^8	
Outer detector hits < 20	2.31×10^8	
Noise event cut 1	2.31×10^8	(796945)
Flash PMT events cut	2.30×10^8	(786745)
VERTEX RECONSTRUCTION		
Second reduction		
Very low energy events cut	1.71×10^8	(786745)
Goodness of fitting cut	1.68×10^8	(786739)
Pre-cut (1.5m, $\sim 5.5\text{MeV}$)	3.27×10^6	(786739)
Noise event cut 2	1.77×10^6	(750930)
SPALLATION CUT		(20% dead time)
Fiducial volume cut (22.5kton)	6.55×10^5	
Energy cut (6.5~20 MeV)	94303	
GAMMA CUT		(7.8% dead time)
Noise event cut 3	67763	(0.15% dead time)
FINAL DATA SAMPLE	65500	

Table 5: The reduction step and the results. Note that the numbers for Monte Carlo are after applying the 22.5kton fiducial cut and 6.5MeV energy cut.

3.2.3 Results

Flux

Fig 9 shows the distribution of the direction of recoil electrons relative to the direction from the sun to the earth for the final data sample. We can see the clear peak towards the sun above background. As the result of the solar neutrino signal extraction, the number of the observed solar neutrino is 4952 signals, and the observed ^8B solar neutrino flux is

$$2.37 \begin{matrix} +0.06 \\ -0.05 \end{matrix} (stat.) \begin{matrix} +0.09 \\ -0.07 \end{matrix} (sys.) \quad [\times 10^6 / cm^2 / sec]. \quad (6)$$

Comparing the result to standard solar models, the ratio of data to SSMs prediction is

$$\frac{Data}{SSM(BP95)} = 0.358 \begin{matrix} +0.009 \\ -0.008 \end{matrix} (stat.) \begin{matrix} +0.014 \\ -0.010 \end{matrix} (sys.) \quad (7)$$

The result shows that the deficit of the solar neutrino flux is very significant if only the experimental errors are taking into account.

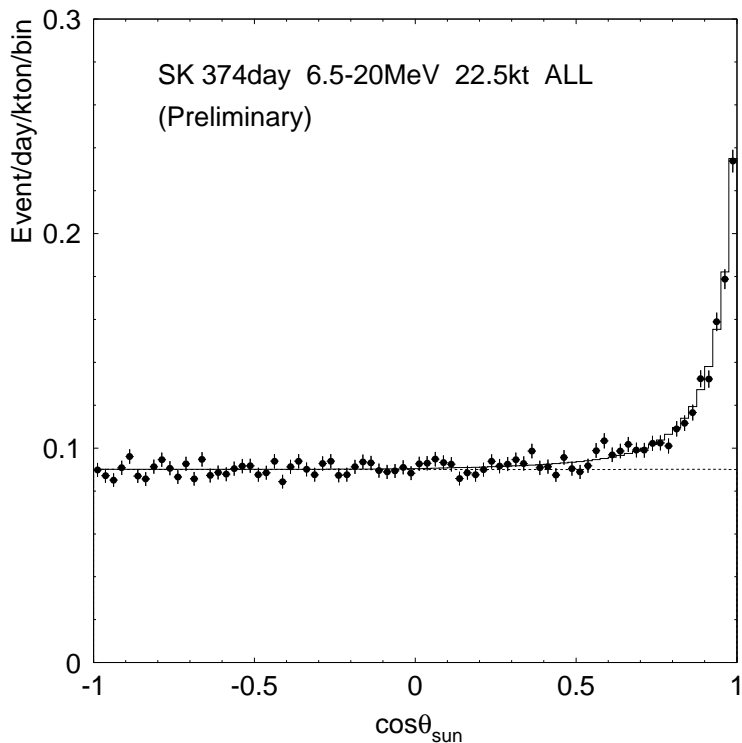


Figure 9: The distribution of the direction of recoil electrons relative to the direction from the sun to the earth.

Day-Night flux variation

We have measured the daytime and the night-time flux separately. The MSW effect, especially the large mixing angle region, makes ν_e regeneration through the earth and flux difference between day and night. If we take the ratio of night-time flux to daytime flux, the analysis for neutrino oscillations becomes independent on solar model calculations. Moreover, this analysis cancels many of the systematic errors. The observed flux is

$$\text{Day} : 2.30 \begin{matrix} +0.08 \\ -0.08 \end{matrix} (stat.) \begin{matrix} +0.09 \\ -0.07 \end{matrix} (sys.) \quad [\times 10^6 / cm^2 / sec]. \quad (8)$$

$$\text{Night} : 2.44 \begin{matrix} +0.08 \\ -0.08 \end{matrix} (stat.) \begin{matrix} +0.10 \\ -0.07 \end{matrix} (sys.) \quad [\times 10^6 / cm^2 / sec]. \quad (9)$$

The relative difference between the daytime and night-time flux is

$$\frac{\text{Day} - \text{Night}}{\text{Day} + \text{Night}} = -0.031 \pm 0.024(stat.) \pm 0.014(sys.). \quad (10)$$

We can not see any differences between daytime and night-time fluxes within the experimental errors.

We have divided the night-time into five bins in terms of the angle between the sun and the Z-axis of the detector as shown in Fig 10. By using this division, we are able to make a sensitive check on the MSW effect which depend on the distance through the earth and the different electron density. Fig 10 also shows the solar neutrino flux in the daytime and the five night-time bins. We can not also see any flux differences between all the bins within the experimental errors.

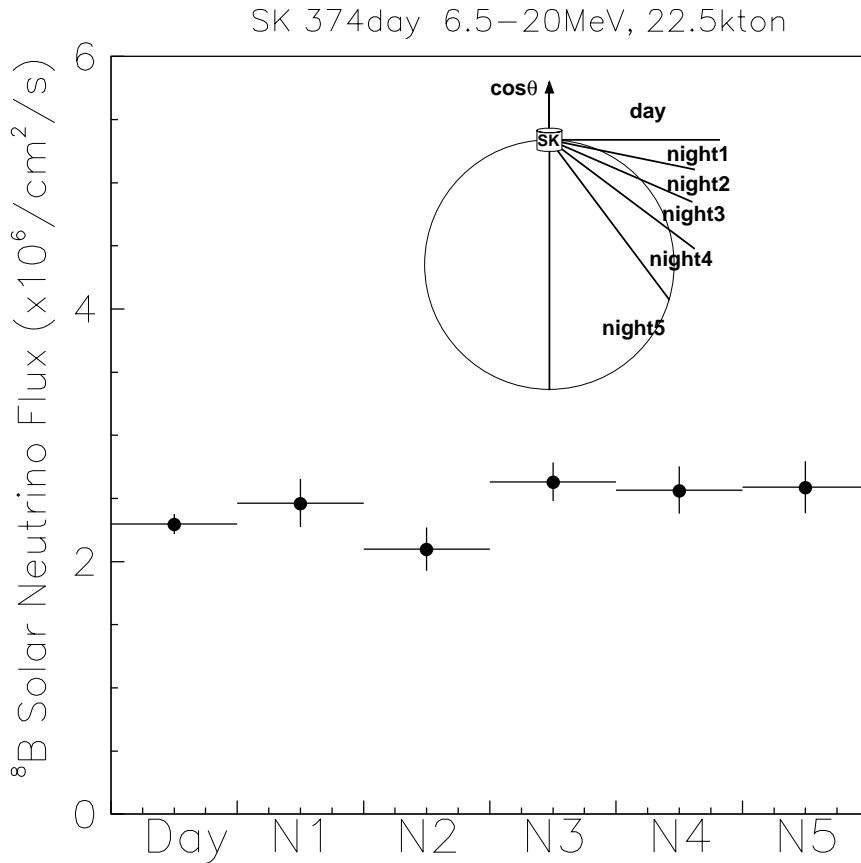


Figure 10: The solar neutrino flux in the daytime and the five night-time bins observed in Super-Kamiokande. The definition of them are also shown.

Seasonal flux variation

The present solar neutrino results cover over one year. Fig 11 shows the solar neutrino flux as a function of time. The orbital eccentricity of the earth causes about 7% flux variation. The measurement is consistent with the expected within the error. This data can be used to study seasonal variation of the solar neutrino flux in which as shown in Fig 11 the just-so oscillation[6] can be studied. The current statistics is unfortunately not very sensitive to check the just-so oscillation, yet.

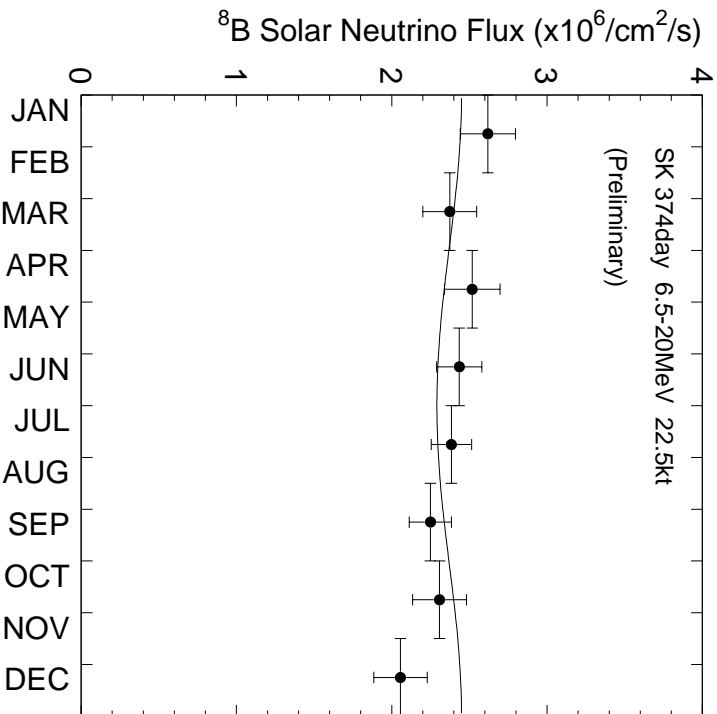


Figure 11: The solar neutrino flux as a function of time.

Energy spectrum

The measurement of the solar neutrino energy spectrum is important, because the shape is solar model independent and sensitive to neutrino oscillations, especially the small angle solution of the MSW effect. Fig 12 shows the ratio of data to SSM prediction in each energy bin. We can see the possibility of the energy distortion, however, it is not significant yet and more statistics is needed. Now, we also need further study the systematic error. The analysis will be very important in the future.

3.3 Implication of the solar neutrino results in Super-Kamiokande

The observed solar neutrino flux is significantly smaller than the predicted value. The solar neutrino problem becomes firm. In this section, the explanation of this problem using MSW effect ($10^{-4} < \sin^2 2\theta < 1, 10^{-8} < \Delta m^2 < 10^{-3} eV^2$) is described. MSW effect is neutrino oscillation in matter of the sun or the earth. In some parameter regions, the flux difference between daytime and night-time would appear. This effect is also non monotonic suppression of neutrinos, so we can see the energy distortion in some parameter regions.

Since the prediction of 8B solar neutrino flux has a large uncertainty, ($6.62 \times 10^6 (1.00^{+0.14}_{-0.17})$ ($\text{cm}^{-2} \text{sec}^{-1}$) in BP95), we performed a flux independent analysis on the Day-Night variation and on the spectrum distortion. From the results of these, we are able to evaluate the excluded regions of the neutrino oscillation parameters. This is shown in Fig 13. Especially, the result of Day-Night variation can exclude about half of the allowed region obtained by the past solar neutrino analyses.

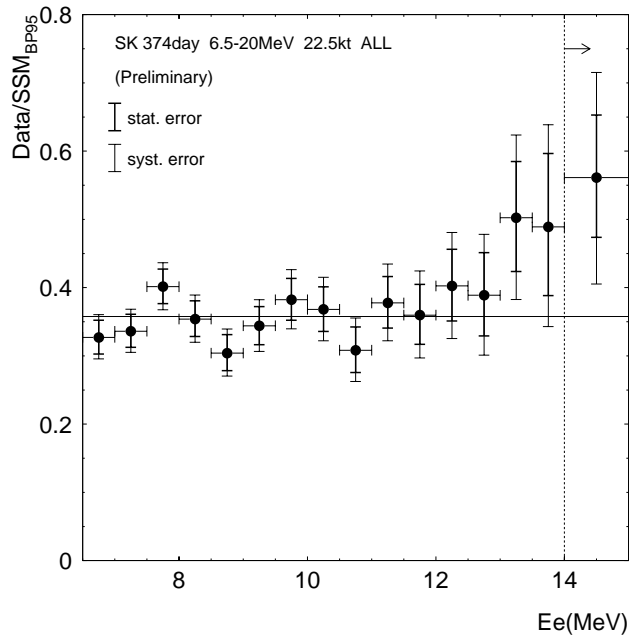


Figure 12: Energy spectrum observed in Super-Kamiokande. Inner and outer error bars shows the statistical and systematic errors, respectively.

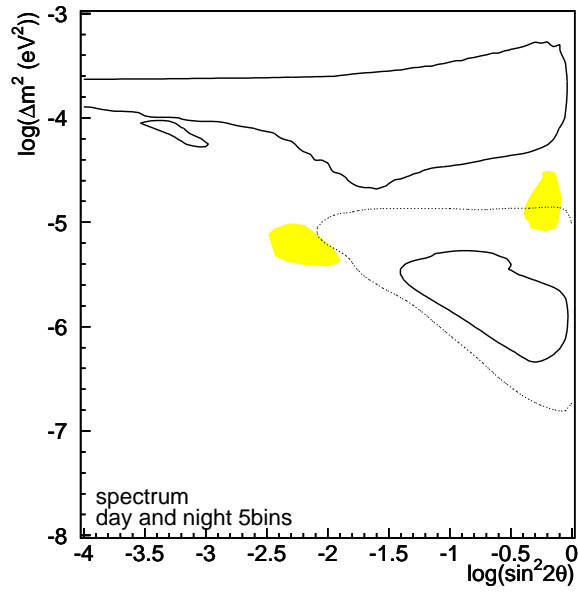


Figure 13: 95% C.L. excluded region at MSW region. Day/Night analysis excludes dotted region and spectrum analysis excludes regions inside of solid lines. Shaded region is the 95% C.L. allowed region from the past solar neutrino experiments by Hata and Langacker[7].

4 Summary

A preliminary result of 25.5 kton·year atmospheric neutrino data in Super-Kamiokande re-confirmed the atmospheric neutrino anomaly. The obtained double ratio, $(\mu/e)_{DATA}/(\mu/e)_{MC}$, is significantly smaller than unity. A strong zenith angle dependence is observed for μ -like events, especially in multi-GeV events. No momentum dependence is observed. The allowed region of neutrino oscillation parameters from the results of atmospheric neutrino data in Super-Kamiokande and Kamiokande is around $\Delta m^2 = 10^{-3} \sim 10^{-2} \text{ eV}^2$ and $\sin^2 2\theta = 0.8 \sim 1.0$.

A preliminary result of 374 days of solar neutrino data in Super-Kamiokande re-confirmed the solar neutrino problem. The observed ^8B solar neutrino flux is

$$2.37 \begin{array}{c} +0.06 \\ -0.05 \end{array} (stat.) \begin{array}{c} +0.09 \\ -0.07 \end{array} (sys.) \quad [\times 10^6 / cm^2 / sec], \quad (11)$$

which is about 36% of the prediction from the standard solar model (BP95). No day-night and seasonal flux variation is seen within the experimental errors. The exclude region of neutrino oscillation parameters is obtained by using the results of day-night flux variation and energy spectrum.

References

- [1] References are in order: M. Aglietta et al., *Europhys. Lett.* 8(1989)611; Ch. Berger et al., *Phys. Lett.* B245(1990)305; K. S. Hirata et al., *Phys. Lett.* B205(1988)416; K. S. Hirata et al., *Phys. Lett.* B280(1992)146; R. Becker-Szendy et al., *Phys. Rev.* D46(1992)3720; W. W. M Allison et al., *Phys. Lett.* B391(1997)491.
- [2] M. Honda et al., *Phys. Rev.* D52(1995)4985.
- [3] J. N. Bahcall et al., *Phys. Rev. Lett.*, **20**, 1209(1968).
- [4] K. Lande Proceedings of the 17th International Conference on Neutrino Physics and Astrophysics, ed. by K. Enqvist et al., World Scientific(1996)25; W. Hampel et al., *Phys. Lett.* B357(1996)384; Results of SAGE I+II+III, private communication with V. N. Gavrin; Y. Fukuda et al., *Phys. Rev. Lett.* 77(1996)1683.
- [5] L. Wolfenstein, *Phys. Rev.*, **D17**, 2369(1978); **D20**, 2634(1979).
S. P. Mikheyev and A. Yu. Smirnov, *Yad. Fiz.* **42**, 1441(1985).
- [6] S. L. Glashow and L. M. Krauss, *Phys. Lett.* **B190**, 199(1988).
P. I. Krastev and S. T. Petcov, *Phys. Rev.*, **D53**, 1665(1996).
- [7] N. Hata and P. Langacker, IASSNS-AST 97/29, UPR-751T(1997).